



## Insight into Janus $V_2COS$ as anode material of high-performance alkali metal ion battery: Diffusion barrier, recyclability, specific capacity, and open-circuit voltage

Fanfan Wang <sup>1</sup>, Jun Yuan,<sup>1</sup> Zhufeng Zhang,<sup>1,\*</sup> Baoan Song,<sup>2</sup> Junhua Zhao,<sup>3</sup> Jincheng Yue,<sup>1</sup> Tian Xu,<sup>4</sup> and Jun Zhou <sup>1,†</sup>

<sup>1</sup>School of Physical Science and Technology, Ningbo University, Ningbo 315211, People's Republic of China

<sup>2</sup>Faculty of Electrical Engineering and Computer Science, Ningbo University, Ningbo 315211, People's Republic of China

<sup>3</sup>College of Chemical and Material Engineering, Quzhou University, Quzhou 324000, People's Republic of China

<sup>4</sup>School of Electronic Information Engineering, Shanghai DianJi University, Shanghai 201306, People's Republic of China



(Received 20 October 2023; accepted 18 July 2024; published 5 August 2024)

Transition metal carbides, nitrides, and carbonitrides, known as MXenes, exhibit exceptional conductivity, stability, and large specific surface area, rendering them promising candidates for anode materials in rechargeable batteries. Herein, we investigate the electrochemical characteristics of the Janus MXene  $V_2COS$  monolayer, as an anode material of alkali metal ion batteries by using first-principles calculations. The phonon band structure and *ab initio* molecular dynamics simulations confirm the stability of the Janus  $V_2COS$  monolayer. The mechanical and electrical properties of the Janus  $V_2COS$  monolayer are explored and proved to have good mechanical stability and electrical conductivity. The surface of the Janus  $V_2COS$  monolayer demonstrates the facile adsorption of alkali metal ions and low diffusion barriers. As an anode material, the recyclability of the Janus  $V_2COS$  has been verified in the ion intercalation/deintercalation processes. Furthermore, the theoretical specific capacities and the open-circuit voltages of the Janus  $V_2COS$  monolayer are calculated to be 165.54 mA h/g and 2.62 V for Li, 662.18 mA h/g and 0.76 V for Na, and 294.43 mA h/g and 0.4 V for K, respectively. It presents that the Janus  $V_2COS$  monolayer is a potential anode material of sodium-ion batteries and potassium-ion batteries.

DOI: [10.1103/PhysRevMaterials.8.085801](https://doi.org/10.1103/PhysRevMaterials.8.085801)

### I. INTRODUCTION

The environmental pollution and the great depletion of traditional fossil fuel sources have produced the urgent need to develop high-efficiency energy storage technology for implementing practice applications of renewable energy sources [1]. Due their the high-power, high-energy density, and long cycle life, as a mainstream alkali metal ion battery, the lithium-ion battery (LIB) has gained widespread use in portable devices, smart electronics, and electric vehicles [2]. However, the rare lithium resources lead to a high production cost of LIBs, which limits the availability of LIBs [3]. In the alkali metal family, lithium, sodium, and potassium have almost the same electronic structure and similar chemical properties. However, abundant sodium and potassium resources offer the advantages of low cost, driving the exploration of sodium-ion batteries (SIBs) and potassium-ion batteries (PIBs) [4–6].

On the other hand, electrode material is a key component of a battery, and its electrochemical properties significantly determine the battery performance. At present, as a commercial anode material, graphite is widely used in LIBs, owing to its good cyclic durability, low cost, and high Coulombic efficiency, but the drawback is the low specific capacity (372 mA h/g) [7]. For SIBs and PIBs, some researches have

presented that graphite is not a suitable anode material due to the less favorable electrochemical property, more significant volume variation (240%–250% for the Na ion and 61% for the K ion), and lower Coulombic efficiency (90% for the Na ion and 54% for the K ion) [8,9]. Consequently, it is necessary to search for a high-quality anode material suitable to SIBs and PIBs.

In recent years, two-dimensional (2D) materials have become a promising anode material, whose large specific surface area provides more electrochemically active sites as well as fast ion diffusion compared to their bulk counterparts [10–14]. Particularly, transition metal carbides, nitrides, and carbonitrides (MXenes) have attracted more attention in the field of energy storage due to their high electronic conductivity, low diffusion barrier, and enhanced charge storage capacity [15–18]. The chemical formula of MXenes is represented by  $M_{n+1}X_nT_x$ , where  $M$  denotes an early transition metal atom (Ti, Zr, Hf, V, etc.),  $X$  is a carbon and/or nitrogen atom,  $T$  denotes the surface termination (such as O, F, OH), and  $n$  can be 1, 2, or 3 [19,20]. As a classical MXene, bare/functionalized  $V_2C$  has been widely studied for its excellent characteristics as an anode material, including a low open-circuit voltage (OCV), and a high theoretical specific capacity. Nyamdelger *et al.* [21] found that the diffusion barrier (0.03 eV) of a Li ion on the  $V_2C$  surface is an order of magnitude smaller than those (0.4–0.5 eV) of the graphene and graphite. Li *et al.* [22] indicated that the adsorption strengths of Li and Na ions on the surface of  $V_2CS_2$  are weaker than that of the surface of  $V_2CO_2$ . Wang *et al.* [23] concluded that both  $V_2CO_2$  and

\*Contact author: zhangzhufeng@nbu.edu.cn

†Contact author: zhoujun@nbu.edu.cn

$V_2CS_2$  exhibit desirable properties as anode materials of PIBs, including a low diffusion barrier, a low OCV, and a high theoretical specific capacity. Thus, the bare/functionalized  $V_2C$  is suggested as a potential electrode material suitable to alkali-metal ion batteries.

Additionally, 2D Janus materials, featuring functionalization on both sides with different atoms, have sparked interest because of their unique structure and physical properties [24–27]. In particular, the inherent mirror asymmetry of 2D Janus materials leads to intrinsic dipole moment, making them more suitable for applications in alkali metal ion batteries [28]. Siriwardane and Hu [29] found that Janus  $Ti_2CS_2Se$  exhibits a higher specific capacity (230.45 mA h/g) and a lower diffusion barrier (0.191 eV), compared to  $M_2CS_2$  ( $M = Zr, Hf, V, Nb, Ta, Mo, \text{ and } W$ ). Özcan and Biel [30] discovered the  $Sc_2CX$  ( $X = N_2, ON, O_2$ ) have different electronic and electrochemical properties, e.g.,  $Sc_2CO_2$  exhibits semiconductor properties and  $Sc_2CN_2$  and  $Sc_2CON$  demonstrate metallic behavior. As the anode materials of SIBs,  $Sc_2CON$  displays a lower diffusion barrier and a lower OCV than those of  $Sc_2CO_2$  and  $Sc_2CN_2$ . Despite the progress made, there remains a scarcity of research regarding Janus MXenes as anode materials of alkali metal ion batteries, necessitating further exploration of their electrochemical performance.

In this paper, based on the favorable electrochemical property of O- or S-terminated MXenes [31], we construct a Janus  $V_2COS$  monolayer as an anode material for alkali metal ion batteries. Here, we first discuss the possibility of experimental preparation of the Janus  $V_2COS$  monolayer. The assumed synthesis process is as follows: In the beginning,  $V_2AlC$  is etched in hydrofluoric acid solution to produce  $V_2CT_x$  ( $T = -O, -OH, \text{ and } -F$  groups) [32]. Then,  $V_2CT_x$  is transformed into  $V_2CO_2$  through a sulfidation/alkalinization treatment [33,34]. Finally,  $V_2CO_2$  undergoes a localized sulfurization treatment to obtain a Janus  $V_2COS$  monolayer [35]. Here, through first-principles calculations, the electrochemical characteristic of the Janus  $V_2COS$  monolayer is evaluated by exploring the diffusion barrier, recyclability, theoretical specific capacity, and OCV during the intercalation/deintercalation processes of alkali-metal ions. The calculation results show that the Janus  $V_2COS$  monolayer can stably adsorb Li, Na, and K ions, and exhibits a low diffusion barrier and a good recyclability. In addition, the calculations of the specific capacity and OCV present that the Janus  $V_2COS$  monolayer is unsuitable to be the anode material of LIBs but favorable to be that of SIBs and PIBs.

## II. COMPUTED METHODS

All calculations are performed by using Quantum Atomstix ToolKit (QATK2021) simulation tools based on density functional theory (DFT) [36]. The electron wave function is expanded by double zeta polarized basis and the density mesh cut-off energy is set to be 75 hartree. The generalized gradient approximation with the Perdew-Burke-Ernzerhof functional is employed to describe the exchange-correlation interactions [37]. Usually, the results calculated by the DFT-D3 method [38] are very close to experimental values [39,40], although the dipole-dipole corrections are limited in precision. Hence,

the DFT-D3 method is chosen in this work for the balance of computational cost and accuracy. A vacuum layer of 30 Å is introduced to avoid unwanted interactions due to the use of periodic boundary conditions. The sampling meshes of Brillouin zones for the unit cell and the  $3 \times 3$  supercell of  $V_2COS$  are set as  $15 \times 15 \times 1$  and  $4 \times 4 \times 1$  by using the Monkhorst-Pack method [41], respectively. During the structure relaxation of  $V_2COS$ , the positions of atoms in the unit cell and the supercell are optimized until the force on each atom converges to less than 0.001 and 0.01 eV/Å, respectively. The effect of spin-orbit coupling (SOC) on the structure and electronic properties of  $V_2COS$  are tested, and the relevant data are listed in Table S1 in the Supplemental Material [42]. The results show that the influence of SOC is almost negligible, therefore the SOC effect is not considered in this work. *Ab initio* molecular dynamics (AIMD) simulations with a Nosé-Hoover heat bath method are employed to examine the stability of Janus  $V_2COS$  at 300 K for 3 ps [43]. The climbing-image nudged elastic band method is adopted to obtain the diffusion barriers and the minimum diffusion paths for alkali metal ions [44]. The finite displacement method is used to calculate the phonon band structure and the atomic displacement is set as 0.01 Å.

## III. RESULTS AND DISCUSSION

### A. Structure and stability of Janus $V_2COS$ monolayer

The constructed Janus  $V_2COS$  monolayer consists of a  $V_2C$  skeleton, an O-terminated surface and a S-terminated surface, as shown in Fig. 1. According to the dual-surface property and the hexagonal crystal symmetry, the Janus  $V_2COS$  monolayer is divided into the four configurations, namely, face centered cubic (fcc), hexagonal close packed (hcp), hybrid face centered cubic and hexagonal close packed (fcc+hcp), and hybrid hexagonal close packed and face centered cubic (hcp+fcc) configurations. In the fcc configuration, O and S atoms are respectively aligned with a V atom, while in the hcp configuration, O and S atoms are aligned with the C atom. In the fcc+hcp configuration, O atoms are placed on top of V atoms, while S atoms are positioned beneath C atoms. Conversely, in the hcp+fcc configuration, O atoms are situated on top of C atoms and S atoms are located below the V atoms. Due to the asymmetrical structure, the Janus  $V_2COS$  monolayer has the space group  $P3m1$  (No. 156), diverging from other MXenes with the space group  $P\bar{3}m1$  (No. 164). The optimized lattice constants of the four configurations of Janus  $V_2COS$  monolayers are 2.93, 2.90, 2.92, and 2.91 Å, respectively, which are close to the values of  $V_2CO_2$  (2.90 Å) and  $V_2CS_2$  (3.06 Å) [23].

First, we calculate the phonon band structures at 0 K to assess the stability of the Janus  $V_2COS$  monolayers. As shown in Fig. 2, the phonon band structures of the Janus  $V_2COS$  monolayer have 15 phonon modes, in which 3 lower frequency modes belong to the acoustic modes and the remaining 12 modes are optical modes. There are some imaginary frequencies in Figs. 2(a) and 2(c), which indicates that the Janus  $V_2COS$  monolayers with the fcc or fcc+hcp configuration are unstable at 0 K. Conversely, there are no imaginary frequencies in Figs. 2(b) and 2(d), which confirms that the Janus  $V_2COS$  monolayers with the hcp or hcp+fcc configuration are

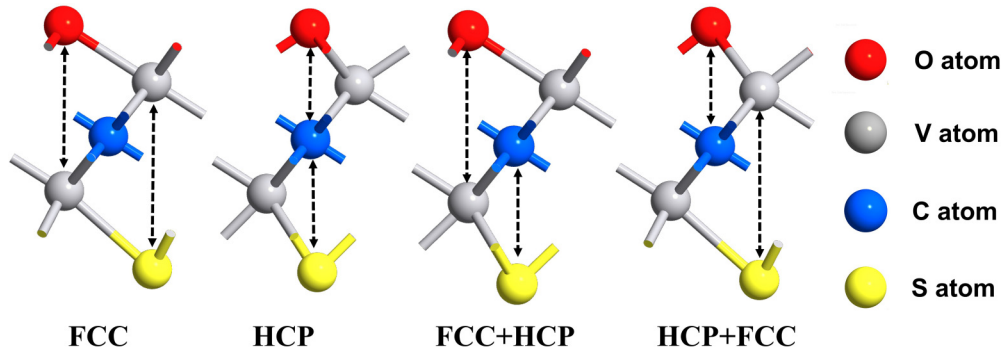


FIG. 1. Side views of Janus  $V_2COS$  unit cell with four configurations: fcc, hcp, fcc+hcp, and hcp+fcc.

dynamically stable. Furthermore, considering the temperature dependence of phonons [45,46], the phonon band structures of the fcc and fcc+hcp configuration at 300 K are also calculated and presented in Fig. S1 in the Supplemental Material [42]. The results show that they are still unstable at 300 K due to the existence of imaginary frequencies. In addition, AIMD simulations are used to examine the thermal stability of the Janus  $V_2COS$  monolayers with the hcp or hcp+fcc configuration at 300 K. As shown in Fig. S2 in the Supplemental Material [42], the Janus  $V_2COS$  monolayers with the hcp or hcp+fcc configuration exhibit a small fluctuation of total energy and no significant structural collapse during the AIMD simulations for 3 ps, which suggests they are thermodynamically stable at room temperature.

To obtain the most stable configuration of Janus  $V_2COS$  monolayer, we investigate the energy change during the following reaction:  $V_2C + S_{\text{bulk}} + O_{\text{gas}} \rightarrow V_2COS$ , representing

the oxygenation and sulfurization of the unterminated  $V_2C$  skeleton. The formation energy ( $E_f$ ) of the Janus  $V_2COS$  monolayer are calculated by the following equation:

$$E_f = E_{V_2COS} - E_{V_2C} - E_O - E_S, \quad (1)$$

where  $E_{V_2COS}$  and  $E_{V_2C}$  denote the total energies of Janus  $V_2COS$  and  $V_2C$ , respectively, and  $E_O$  represents a half of the total energy of  $O_2$  in the gas phase, and  $E_S$  corresponds to the total energy of S in its bulk material. For the hcp and hcp+fcc configurations, the calculated  $E_f$  is  $-8.24$  and  $-8.42$  eV, respectively. As well known, a negative  $E_f$  indicates an exothermic reaction, meaning that the Janus  $V_2COS$  is stable against decomposition into S bulk,  $O_2$  in the gas phase, and unterminated  $V_2C$  monolayer. Consequently, the Janus  $V_2COS$  monolayer with the hcp+fcc configuration is further studied in subsequent works due to its lower  $E_f$  and greater stability.

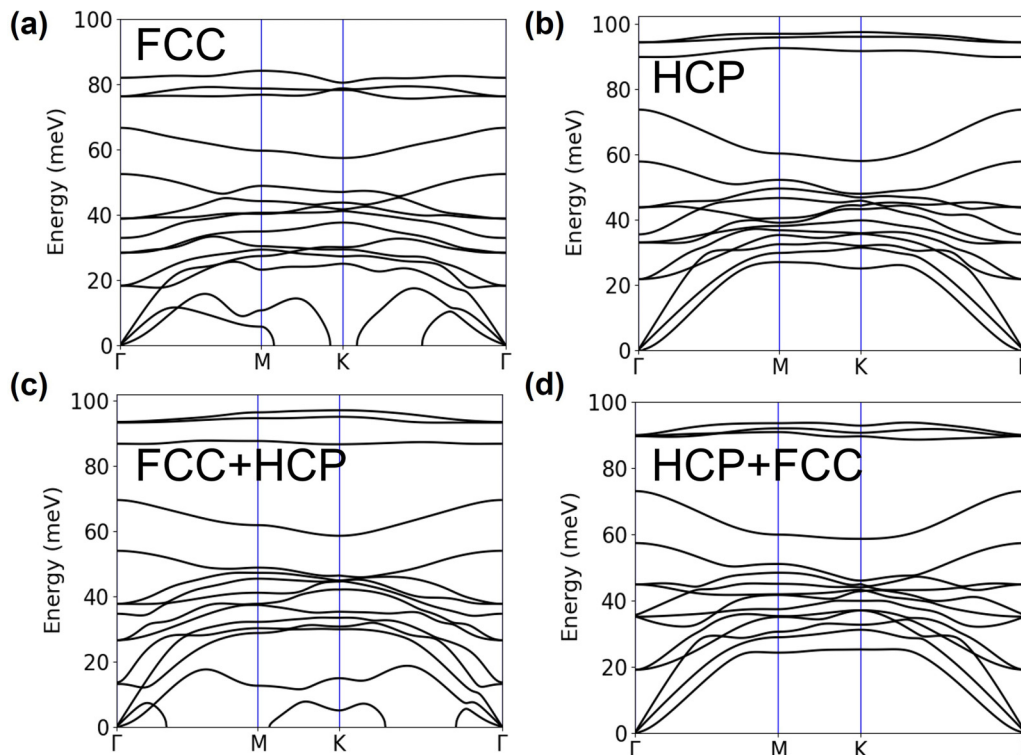


FIG. 2. Phonon band structure of the Janus  $V_2COS$  monolayer with (a) fcc, (b) hcp, (c) fcc+hcp, and (d) hcp+fcc configurations.

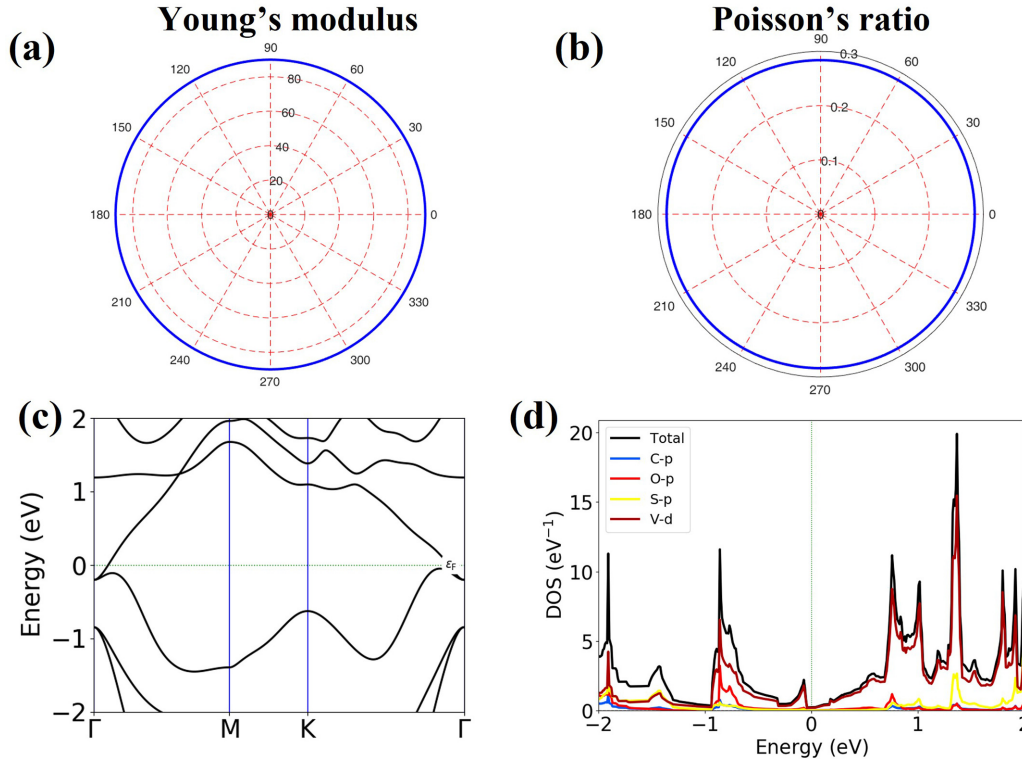


FIG. 3. (a) Young's modulus, (b) Poisson's ratio, (c) band structure, and (d) projected density of states of the Janus  $V_2COS$  monolayer.

### B. Mechanical and electronic properties of Janus $V_2COS$ monolayer

First, the strain-stress method is used to calculate the elastic constant of the Janus  $V_2COS$  monolayer, as described in Note 1 of the Supplemental Material [42]. The calculated elastic constants are  $C_{11} = C_{22} = 97.82$  GPa,  $C_{12} = 27.75$  GPa, and  $C_{66} = 35.04$  GPa. Apparently, they

satisfy the Born mechanical stability criteria ( $C_{11} > 0$ ,  $C_{12} > 0$ , and  $C_{11} > |C_{12}|$ ) [47], proving the mechanical stability of the Janus  $V_2COS$  monolayer.

Second, the orientation-dependent Young's modulus  $Y(\theta)$  and Poisson's ratio  $\nu(\theta)$  are used to evaluate the deformation feature of the Janus  $V_2COS$  monolayer. The formulations of  $Y(\theta)$  and  $\nu(\theta)$  follow as [48]

$$Y(\theta) = \frac{C_{11}C_{12} - C_{12}^2}{C_{11}\sin^4(\theta) + C_{22}\cos^4(\theta) + \left[ \frac{C_{11}C_{22} - C_{12}^2}{C_{66}} - 2C_{12} \right] \cos^2(\theta)\sin^2(\theta)}, \quad (2)$$

$$\nu(\theta) = \frac{\left( C_{11} + C_{12} - \frac{C_{11}C_{22} - C_{12}^2}{C_{66}} \right) \cos^2(\theta)\sin^2(\theta) + C_{12}(\sin^4(\theta) + \cos^4(\theta))}{C_{11}\sin^4(\theta) + C_{22}\cos^4(\theta) + \left[ \frac{C_{11}C_{22} - C_{12}^2}{C_{66}} - 2C_{12} \right] \cos^2(\theta)\sin^2(\theta)}, \quad (3)$$

where  $\theta$  denotes the angle between the strain direction and the  $x$  axis. As shown in Figs. 3(a) and 3(b), the Young's modulus  $Y(\theta)$  and the Poisson's ratio  $\nu(\theta)$  of the Janus  $V_2COS$  monolayer are independent of  $\theta$  and exhibit isotropic properties. Moreover, the Young's modulus (88.5 GPa) of the Janus  $V_2COS$  monolayer is higher than that of other 2D materials, such as  $C_3Al$  (61.61 GPa) and  $C_7N_2$  (68.13 GPa) [49,50], which ensures greater strength and stiffness. The Poisson's ratio of 0.29 is lower than that of other Janus MXenes, such as  $Ti_2CSO$  (0.318) and  $Sc_2CON$  (0.338) [29,30]. A low Poisson's ratio signifies a small stress and deformation stemming from transverse expansion during the intercalation/deintercalation process of alkali metal ions, which is a

desired result to enhance the stability and lifespan of the battery.

As is well known, the electrical conductivity is a critical factor for the electrochemical performance of anode materials. We calculate the band structure and projected density of states (PDOS) of the Janus  $V_2COS$  monolayer to analyze its electronic properties. As shown in Figs. 3(c) and 3(d), the Janus  $V_2COS$  monolayer displays metallic properties, and the density of states dominated by the  $3d$  orbitals of the V atom crosses the Fermi energy level, which is similar with the cases of  $V_2C$ ,  $V_2CO_2$ , and  $V_2CS_2$  [51]. It demonstrates the Janus  $V_2COS$  monolayer has good electrical conductivity to be an anode material.



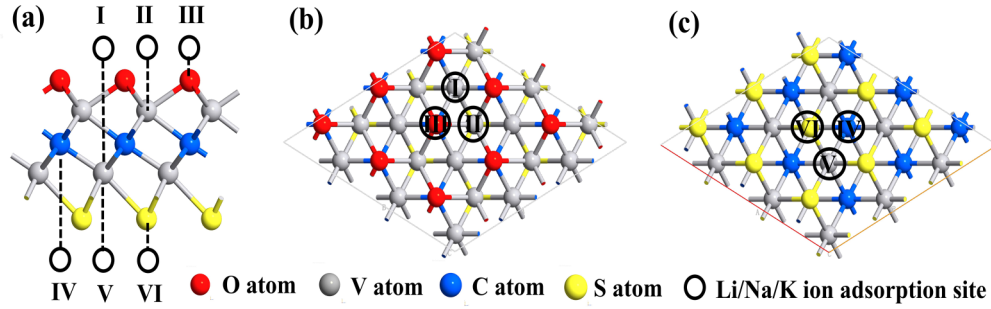


FIG. 4. (a) Side view, (b) top view, and (c) bottom view of the six possible kinds of adsorption sites (site I, site II, site III, site IV, site V, and site VI).

### C. Adsorption characteristics of single alkali metal ion

The adsorption characteristic of an alkali metal ion is particularly important for selecting an anode material. A  $3 \times 3 \times 1$  V<sub>2</sub>COS supercell is constructed to study the adsorption of a single Li/Na/K ion on the surface of Janus V<sub>2</sub>COS monolayer. As shown in Fig. 4, there are six possible adsorption sites (sites I–VI) on the O- and S-terminated surfaces of the V<sub>2</sub>COS supercell. In Figs. 4(a) and 4(b), site I and site II align with the lower-layer and the upper-layer V atoms, respectively, and site III aligns with the O atom. In Figs. 4(a) and 4(c), sites IV and V align with the C and V atoms, respectively, and site VI is right under a S atom. To evaluate the adsorption stability of an alkali metal ion, the adsorption energy ( $E_{\text{ad}}$ ) of the adsorption site is calculated by the following equation:

$$E_{\text{ad}} = E_{V_2\text{COSA}} - E_{V_2\text{CSO}} - E_A \quad (A = \text{Li/Na/K}), \quad (4)$$

where  $E_{V_2\text{COSA}}$  is the total energy of the V<sub>2</sub>COS supercell adsorbed by an alkali metal ion,  $E_{V_2\text{CSO}}$  denotes the total energies of the Janus V<sub>2</sub>COS supercell, and  $E_A$  represents the total energy of an atom in the body-centered-cubic structure of bulk Li/Na/K. It is worth pointing out that  $E_A$  in Eq. (4) should be calculated by the Perdew-Burke-Ernzerhof method without considering DFT-D3 correction because the DFT-D3 method often leads to unphysical results [52].

According to Eq. (4), a negative adsorption energy represents an exothermic reaction and an attractive interaction between an alkali-metal ion and the Janus V<sub>2</sub>COS supercell. For the above six sites, the calculated adsorption energies are listed in Table I. From Table I, it can be observed that for all the alkali metal ions, the adsorption energy of site II is consistently lower than that of sites I and III. Therefore, we can deduce that the alkali metal ions are always preferentially adsorbed on site II located at the O-terminated surface of the V<sub>2</sub>COS supercell. Similarly, the alkali metal ions prefer to adsorb at site V on the S-terminated surface of the V<sub>2</sub>COS supercell.

TABLE I. Adsorption energy of single Li/Na/K ion.

	Site I	Site II	Site III	Site IV	Site V	Site VI
Li	-3.69 eV	-3.79 eV	-2.63 eV	-1.52 eV	-1.71 eV	-0.52 eV
Na	-3.43 eV	-3.59 eV	-2.58 eV	-1.41 eV	-1.42 eV	-0.8 eV
K	-3.62 eV	-3.71 eV	-1.58 eV	-1.64 eV	-1.65 eV	-1.41 eV

Furthermore, the electron density difference (EDD) is calculated to demonstrate the adsorption behavior of alkali-metal ions at sites II and V. The EDD is defined as the variation of electron density before and after the alkali-metal ion adsorbed on the O- and S-terminated surfaces and presented as follows:

$$\Delta\rho = \rho_{V_2\text{COSA}} - \rho_{V_2\text{CSO}} - \rho_A \quad (A = \text{Li/Na/K}), \quad (5)$$

where  $\rho_{V_2\text{COSA}}$ ,  $\rho_{V_2\text{CSO}}$ , and  $\rho_A$  denote the electron densities of the V<sub>2</sub>COS supercell adsorbed Li/Na/K ion, pristine V<sub>2</sub>COS supercell, and Li/Na/K atom, respectively. As shown in Fig. 5, the azure region indicates the electron depletion and the purple region illustrates the electron accumulation. It can be noticed from Fig. 5 that the electrons transfer from an alkali metal ion to the O- or S-terminated surfaces of Janus V<sub>2</sub>COS monolayer and mainly gather between the adsorbed alkali metal ions and its adjacent O or S atoms.

Moreover, the Mulliken population analyses are calculated to quantitatively gain insight into the electrons transfer behavior [53,54]. The amounts of electron transfer are shown in Fig. 5. It can be found that the alkali metal ions always transfer more electrons to O-terminated surfaces while less electrons to S-terminated surfaces, which can be attributed to the fact that the O atom has fewer electron shells and a stronger capability of attracting electrons. The magnitudes of electrons transferred from Na and K ions to the Janus V<sub>2</sub>COS monolayer are almost equal, that is,  $0.68e$  and  $0.67e$  for the S-terminated surface, and  $0.94e$  and  $0.95e$  for the O-terminated surface. However, the magnitude of electrons transferred from the Li ion to the Janus V<sub>2</sub>COS monolayer is notably small compared with that of the Na and K ions. This small electron transfer can be attributed to the strong attraction between the nuclei of the Li atom and its valence electrons, making it difficult for the electrons to escape.

To review the conductivity of the Janus V<sub>2</sub>COS monolayer adsorbed Li/Na/K ion, the PDOS are calculated and shown in Fig. S3 in the Supplemental Material [42]. It can be explicitly seen that the Janus V<sub>2</sub>COS monolayer adsorbed alkali metal ion still exhibits a metallic nature. Comparing with the density of states of the pristine Janus V<sub>2</sub>COS monolayer [Fig. 3(d)], the Janus V<sub>2</sub>COS monolayer with the Li/Na/K ion exhibits a higher density of states at the Fermi energy level, which ensures an excellent electrical conductivity. Therefore, in terms of the adsorption stability and conductivity, the V<sub>2</sub>COS monolayer can serve as a prospective anode material of alkali-metal ion batteries.

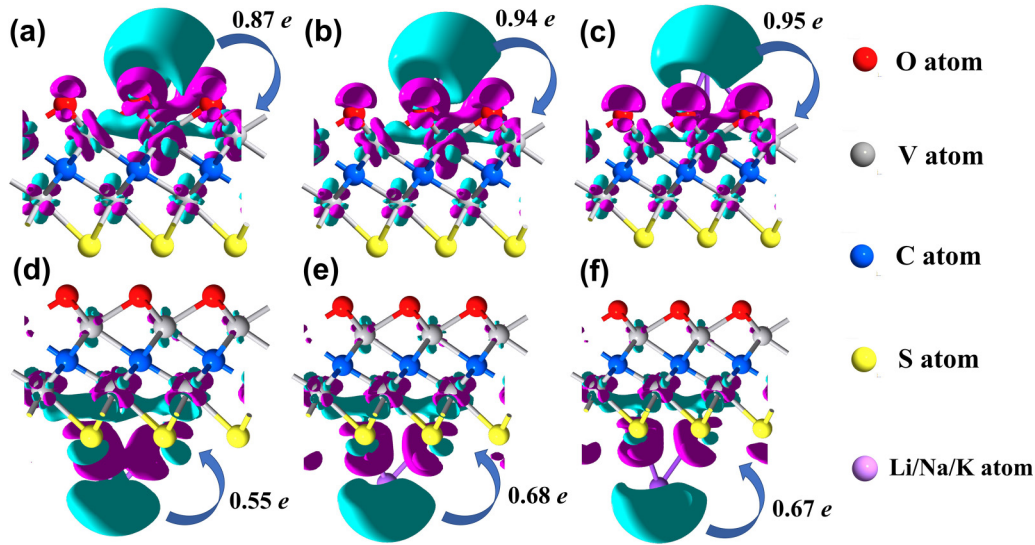


FIG. 5. Charge density difference of the most stable adsorption site on the O- and S-terminated surfaces of the Janus  $V_2COS$  supercell: site II for the (a) Li, (b) Na, and (c) K ion; site V for the (d) Li, (e) Na, and (f) K ion. (Isovalue =  $0.001e/\text{\AA}^3$ ).

#### D. Alkali-metal ionic diffusion characteristic

The charge/discharge rate of an alkali metal ion battery correlates closely with the diffusion velocity of the ion on the surface of the anode material, while a low diffusion barrier indicates a fast diffusion velocity of the ion [55]. Given the presence of two distinct surfaces of Janus  $V_2COS$  monolayer, we compute the diffusion barrier of a single Li/Na/K ion on the O- and S-terminated surfaces, respectively.

Based on the structure symmetry of the Janus  $V_2COS$  monolayer, there are two possible paths for the migration of an alkali metal ion on each surface. As depicted in Fig. 6, path 1 ( $A \rightarrow A'$ ) involves the direct migration of an alkali metal ion from a stable adsorption site (site II or site V) to an adjacent stable adsorption site (site II or site V), while path 2 ( $A \rightarrow B \rightarrow A'$ ) denotes the alkali metal ion transfers first from a stable adsorption site (site II or site V) to an adjacent sub-stable adsorption site (site I or site IV), and then to another stable adsorption site (site II or site V). Along the above-described migration paths, the diffusion energy profiles of a Li/Na/K ion on the O- and S-terminated surfaces are calculated and shown in Fig. 7, respectively. It is clearly observed that, for all the alkali metal ions on the O- and S-terminated surfaces, path 2 consistently exhibits a lower diffusion barrier. Among the three alkali metal ions, the K ion has the smallest

diffusion barrier, while the Li ion has the largest diffusion barrier. However, the diffusion barrier for all the alkali metal ions is lower than that of a commercial graphite-based LIB (0.48 eV) [56]. Apparently, the diffusion barriers of the Li/Na/K ion on the surface of the Janus  $V_2COS$  monolayer are comparable to that of the ions on the surface of  $V_2CO_2$  monolayer and  $V_2CS_2$  monolayer [20,21,57].

A diffusion coefficient is another significant index to evaluate the charge/discharge rate of an alkali metal ion battery. Based on the transition state theory, the diffusion coefficient can be computed by the following equation [58]:

$$D = d^2 \omega / \exp\left(\frac{E_a}{k_B T}\right), \quad (6)$$

where  $d$  represents the diffusion distance,  $\omega$  is the attempt frequency,  $E_a$  denotes the diffusion barrier, and  $k_B$  and  $T$  are the Boltzmann's constant and the absolute temperature, respectively. At room temperature,  $\omega$  taken as  $10^{13}$  Hz [59], the diffusion coefficients of the Li, Na, and K ions on the O-terminated surface of the Janus  $V_2COS$  monolayer are calculated to be  $1.17 \times 10^{-6}$ ,  $3.72 \times 10^{-6}$ , and  $3.78 \times 10^{-5}$   $\text{cm}^2/\text{s}$ , respectively, while on the S-terminated surface, the diffusion coefficients of the Li, Na, and K ions are  $7.8 \times 10^{-8}$ ,  $8.2 \times 10^{-5}$ , and  $1.23 \times 10^{-3}$   $\text{cm}^2/\text{s}$ . Obviously, the K ion has

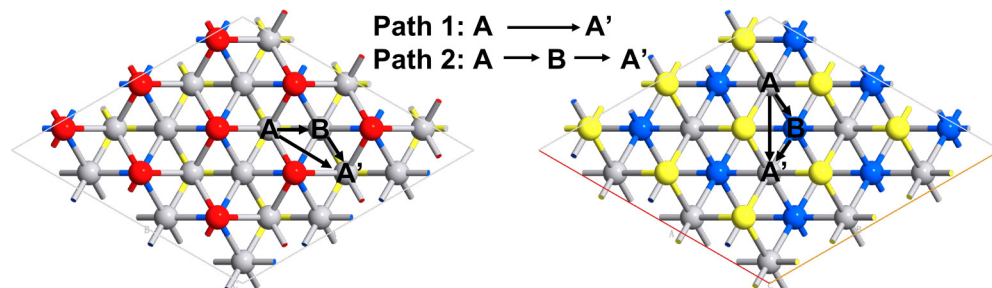


FIG. 6. Diffusion paths for Li/Na/K ions adsorbed on the O- and S-terminated surfaces of the Janus  $V_2COS$  monolayer.

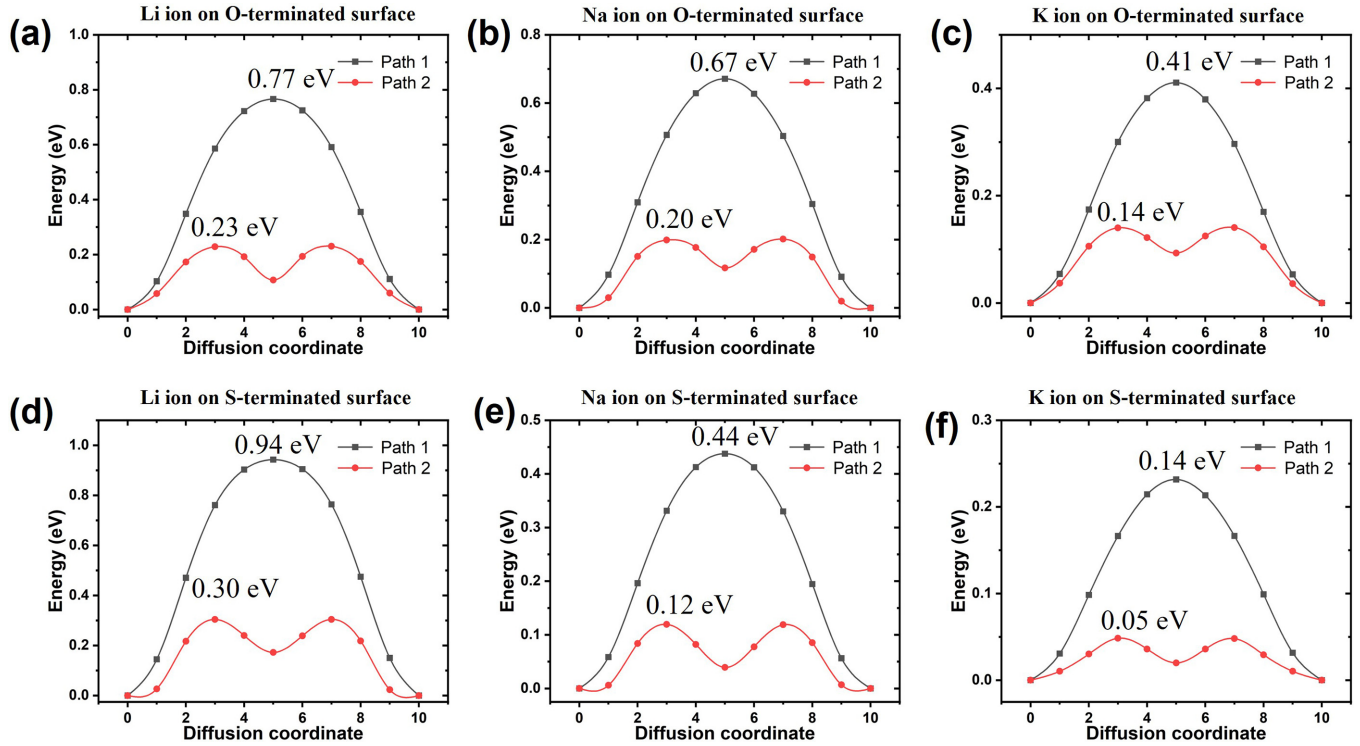


FIG. 7. Diffusion barrier of a single alkali metal ion on the surface of the Janus V<sub>2</sub>COS monolayer.

the largest diffusion coefficient, that is, K ions have the fastest diffusion velocity on the surface of the Janus V<sub>2</sub>COS monolayer.

### E. Multilayer adsorption of alkali metal ions

Investigating the multilayer adsorption behavior of alkali-metal ions offers a comprehensive understanding of the charge storage mechanism and capacity limitation in a rechargeable battery. In the beginning, the alkali metal ions are adsorbed at site II one by one because site II is the most stable site. When all 9 site II on the O-terminated surface of  $3 \times 3 \times 1$  V<sub>2</sub>COS supercell are filled, the first adsorption layer is formed. Then the  $E_{ad}$  of the adsorption sites are tested to determine the most stable adsorption site of the second adsorption layers. When the most stable adsorption sites are filled by the ions, the second adsorption layer with the lowest energy state is formed. Repeating the above process, the subsequent adsorption layers are formed in turn (see Note 2, Table S2, and Fig. S4 in the Supplemental Material [42]).

At the same time, the ability of multilayer adsorption of alkali metal ions is evaluated by the average adsorption energy of each layer. The average adsorption energy is calculated by following equation [60]:

$$E_{av} = \frac{(E_{V_2COS A_x} - E_{V_2COS A_{x-n}} - nE_A)}{n} \quad (A = \text{Li/Na/K}), \quad (7)$$

where  $E_{V_2COS A_x}$  denotes the total energy of the V<sub>2</sub>COS supercell with  $x$  adsorbed ions,  $n$  is the number of ions in the outermost adsorption layer, and  $E_A$  is the same as the definition in Eq. (4). For a multilayer adsorption configuration,  $E_{av}$  dependent on the number of adsorbed ions is shown in

Fig. 8(a). It can be noticed that the  $E_{av}$  changes to positive when the number of Li, Na, and K ions is larger than 27, 54, and 15, respectively. This means the number of adsorbable ions reaches maximum because a positive  $E_{av}$  presents an unstable adsorption.

Further, we calculate the electron location function (ELF) of the V<sub>2</sub>COS supercell with multilayer adsorption ions to analyze the adsorption behavior of alkali metal ions. As shown in Fig. 8(b), for the adsorption configuration of the Li ion, there exists a continuous negative electron cloud (NEC) outside the Li ion on the O-terminated surface, but the electrons around the Li ions on the S-terminated surface exhibit significant localization and lack a continuous NEC. For the adsorption configuration of the Na ion, all the neighboring adsorption layers are surrounded by a NEC. The NEC serves as an additional cohesive force for the adsorbed alkali metal ions, effectively screening the Coulomb repulsive forces between the alkali-metal ions and enhancing the adsorption stability of the ions [61]. Hence, the lack of NEC makes it hard for the Li ion to be adsorbed on the S-terminated surface. In contrast, a multilayer of Na ions can be stably adsorbed on both surfaces of the Janus V<sub>2</sub>COS monolayer due to the uniform NEC. The formation of a NEC can be attributed to the overlapping of valence electrons of alkali metal ions with the increase of adsorbed ions. For the adsorption configuration of the K ion, there is a higher concentration NEC covering the adsorbed K ion layer due to its larger radius and the overlapping of more valence electrons. Even more significantly, there is a higher ELF value between adjacent K ions adsorbed on the S-terminated surface, which indicates that K ions are too close, resulting in a strong repulsion between them.



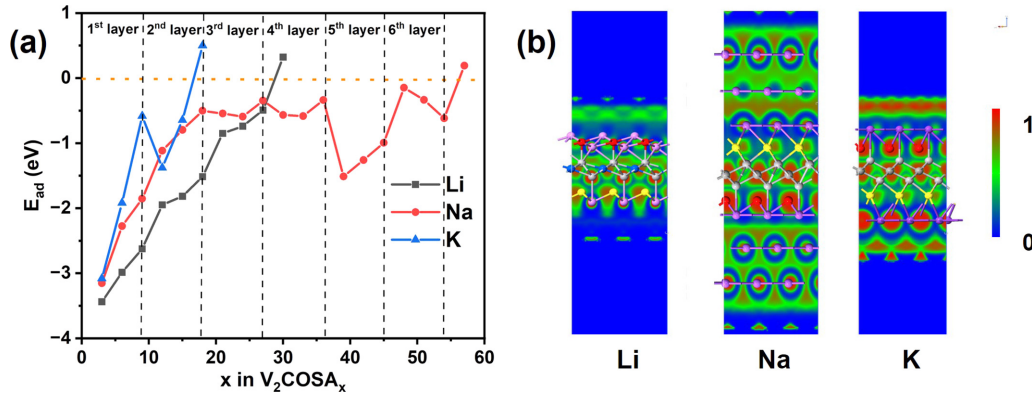


FIG. 8. (a) Average adsorption energy ( $E_{\text{av}}$ ) dependent on the number of Li/Na/K ions; (b) the electron location function of the Janus  $\text{V}_2\text{COS}$  monolayer with 27 Li ions, 54 Na ions, and 15 K ions, respectively.

### F. Recyclability and dipole moment

In fact, the deformation of anode materials is a common phenomenon during the ion intercalation process. The deformation restorability determines the cycle life of the alkali metal ion battery. In the intercalation process of ions, the anode material deforms due to volume expansion. Here, the ratio of volume expansion  $\eta$  is defined as the ratio of volume increment  $\Delta V$  and origin volume  $V_0$ :

$$\eta = \frac{\Delta V}{V_0} = \frac{V_1 - V_0}{V_0}, \quad (8)$$

where  $V_1$  is the volume after expansion. For the Janus  $\text{V}_2\text{COS}$  monolayer, Fig. 9(a) shows the ratio of volume expansion with the intercalation number of alkali metal ions. It is found that the expansion deformation gradually increases with the intercalation number of alkali metal ions. When nine alkali metal ions are intercalated, the ratio of volume expansion of the Janus  $\text{V}_2\text{COS}$  monolayer is 8.3%, 6.9%, and 9.4% for the Li, Na, and K ions, respectively. They are lower than that of most of 2D materials, such as  $\text{SnS}_2$  (11.7%) [62] and  $\text{MoS}_2$  (15%–20%) [63]. However, from Fig. 9(a), when the numbers of Li ions and Na ions exceeds 9 and 36, respectively, the volume of the Janus  $\text{V}_2\text{COS}$  monolayer rapidly expands to cause a large structure change, and an increased  $\eta$  beyond 30%. According to Zhang's suggestion, it is better that the

volume deformation of the electrode material should be lower than 25% to ensure a long cycle life of the alkali metal ion battery [64]. Hence, it can result in the intercalation number of Li, Na, and K ions being respectively lower than 9, 36, and 15, to make a small volume expansion of the Janus  $\text{V}_2\text{COS}$  anode material.

To assess the reversibility of recharge/discharge cycles, the deformation restorability of Janus  $\text{V}_2\text{COS}$  is tested using AIMD simulations with an  $NVT$  canonical ensemble. First, the intercalated alkali metal ions causing the structure change are removed. Subsequently, the AIMD simulation is performed for the deformed Janus  $\text{V}_2\text{COS}$  monolayer and shown in Fig. S5 in the Supplemental Material [42]. It is found that the Janus  $\text{V}_2\text{COS}$  monolayer recovers its initial structure at 300 K after AIMD simulations for 3 ps, suggesting a good recyclability of the Janus  $\text{V}_2\text{COS}$  monolayer as an anode material.

On the other hand, the intrinsic dipole moment is an important characteristic of the asymmetric structure of the Janus  $\text{V}_2\text{COS}$  monolayer with the uneven distribution of electrons. Due to the stronger electronegativity of O atoms, the O atoms attract more electrons from the neighboring V atoms, while the S atoms get relatively fewer electrons from the neighboring V atoms, which results in an intrinsic dipole moment of 2.9 De pointing from the S-terminated surface to the

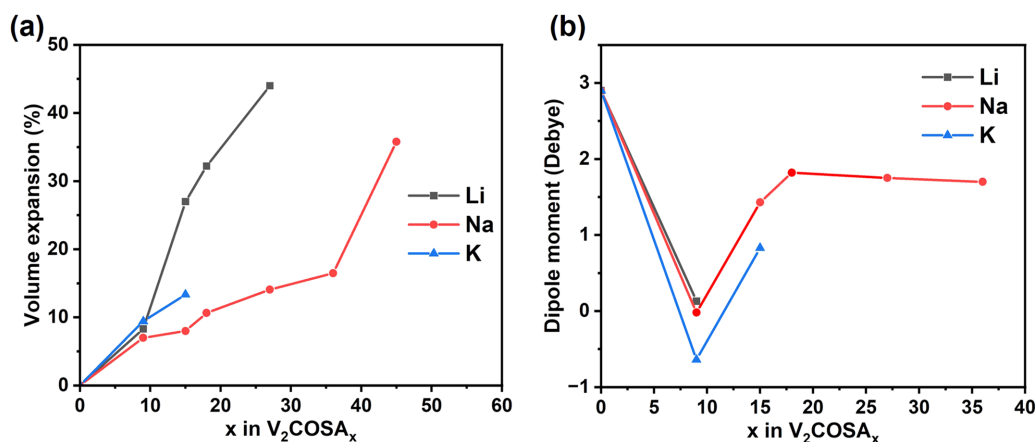


FIG. 9. (a) Volume expansion and (b) dipole moment of the Janus  $\text{V}_2\text{COS}$  monolayer dependent on the number of Li/Na/K ions.



TABLE II. Specific capacity of 2D anode materials for Li, Na, and K ions.

Materials	Li (mA h/g)	Na (mA h/g)	K (mA h/g)
Graphite	372 [7]	111.7 [8]	273 [9]
MoS <sub>2</sub>	680 [10]	530 [11]	100 [12]
V <sub>2</sub> CO <sub>2</sub>	367.4 [22]	367.4 [22]	489.9 [23]
V <sub>2</sub> CS <sub>2</sub>	301.1 [22]	301.1 [22]	200.2 [23]
V <sub>2</sub> CSe <sub>2</sub> [66]		394.12	394.12
Cr <sub>2</sub> CO <sub>2</sub> [67]	330.9	276.3	
WSSe [68]	477.8	371.5.42	156.0
MoSSe	776.5 [69]	510 [70]	203 [70]
V <sub>2</sub> COS (this work)	165.54	662.18	294.43

O-terminated surface. The total dipole moments of the Janus V<sub>2</sub>COS monolayer with alkali metal ions are calculated and shown in Fig. 9(b). Obviously, the total dipole moment is intensively dependent on the number of adsorbed alkali metal ions, especially in the case of less adsorbed ions. With increasing the adsorbed ions, there is no significant change of the total dipole moment due to the slight effect of the more adsorbed Na ions on the electron distribution.

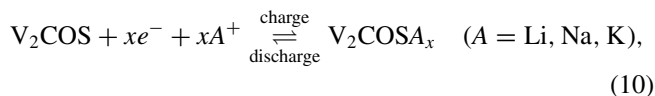
### G. Specific capacity and open-circuit voltage

Now, we investigate the specific capacity and the open-circuit voltage (OCV) of the Janus V<sub>2</sub>COS monolayer as an anode material for evaluating the essential characteristic of an alkali metal ion battery. The specific capacity of the Janus V<sub>2</sub>COS monolayer is calculated by the following equation [65]:

$$C_M = \frac{x_{\max} * z * F}{M}, \quad (9)$$

where  $z$  is the number of valence electrons of the alkali metal ion ( $z = 1$  for Li, Na, and K),  $x_{\max}$  is the maximum number of adsorbed alkali metal ions ensuring the recyclability of the electrode (here,  $x_{\max} = 9, 36,$  and  $15$  for Li, Na, and K ions, respectively),  $F$  is the Faraday constant ( $F = 26\,810$  mA h/mol), and  $M$  represents the molar mass of the anode material. In terms of the  $3 \times 3 \times 1$  Janus V<sub>2</sub>COS supercell,  $M = 1457.55$  g/mol,  $C_M = 165.54, 662.18,$  and  $275.91$  mA h/g for Li, Na, and K ions, respectively. Obviously, the specific capacity of the Janus V<sub>2</sub>COS monolayer is the highest for the Na ion. As summarized in Table II, the specific capacity of the Janus V<sub>2</sub>COS monolayer for the Li ion is smaller than that of most of the 2D materials; for the Na ion, the specific capacity of the Janus V<sub>2</sub>COS monolayer is the largest; for the K ion, the specific capacity is larger than that of MoS<sub>2</sub> and V<sub>2</sub>CS<sub>2</sub>, but smaller than that of V<sub>2</sub>CO<sub>2</sub> and V<sub>2</sub>CSe<sub>2</sub>.

In the charge-discharge process of an alkali metal ion battery, the chemical reactions of ion intercalation and deintercalation are presented as the following equation:



where  $x$  denotes the number of alkali metal ions adsorbed on the Janus V<sub>2</sub>COS supercell. As shown in Eq. (10), the alkali

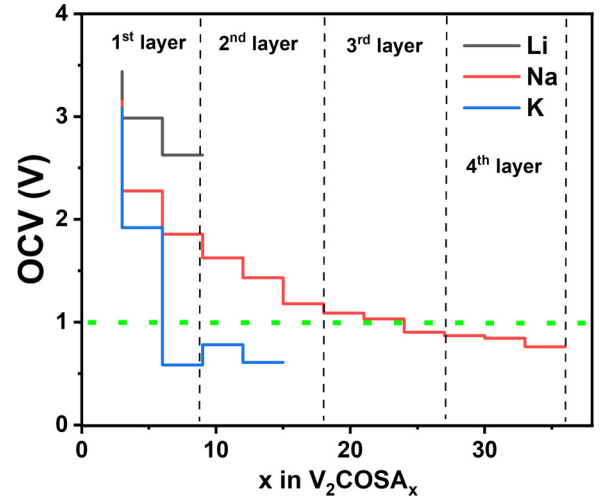


FIG. 10. Open-circuit voltage of the Janus V<sub>2</sub>COS monolayer dependent on the number of Li/Na/K ions.

metal ions and electrons intercalate into Janus V<sub>2</sub>COS during charge, and the alkali metal ions deintercalate from the anode material during discharge. Based on the above process, the OCV can be calculated as the following equation [71,72]:

$$OCV \approx -\frac{E_{V_2COSA_x} - E_{V_2COS} - xE_A}{xe}, \quad (11)$$

where  $E_{V_2COSA_x}$  and  $E_{V_2COS}$  are total energies of the Janus V<sub>2</sub>COS monolayer with and without alkali metal ions, respectively, and  $x$  denotes the number of alkali metal ions and  $E_A$  represents the total energy of an alkali metal atom in the bulk material. The open-circuit voltages of the Janus V<sub>2</sub>COS monolayer for different numbers of adsorbed Li/Na/K ions are calculated and plotted in Fig. 10. As shown in Fig. 10, the OCVs gradually decrease with an increasing number of adsorbed alkali metal ions. When the number of adsorbed Li, Na, and K ions reaches maximum, i.e., 9, 36, and 15, their OCVs are 2.62, 0.76, and 0.4 V, respectively. In general, the reference OCV of anode material is set to be in range of 0–1 V for effectively avoiding the formation of dendrite during the charging/discharging process [73]. As an obvious result, the higher OCV for the Li ion (2.62 V) makes the Janus V<sub>2</sub>COS monolayer not suitable as an anode material for LIB. However, the lower OCV for the Na ion (0.76 V) and the K ion (0.4 V) can provide a high operating voltage for SIBs and PIBs [74]. It demonstrates that the Janus V<sub>2</sub>COS monolayer as an anode material is suitable for a high-capacity SIB and a high-voltage PIB. In addition, it is worth mentioning that as an anode material for SIBs and PIBs, Janus V<sub>2</sub>COS should be loaded on carbon cloth or metal foil [75,76] to enhance the stability and conductivity of the entire electrode.

## IV. CONCLUSION

In summary, we construct a Janus V<sub>2</sub>COS monolayer and confirm its stability by the analysis of the phonon band structure, AIMD simulation, and formation energy. The mechanical property and electrical conductivity of the Janus V<sub>2</sub>COS monolayer are systematically investigated to evaluate its potential as an anode material of alkali metal ion batteries.

The calculation of adsorption energy shows that alkali metal ions can be stably adsorbed on the surface of the Janus  $V_2COS$  monolayer. Compared to the S-terminated surface of the Janus  $V_2COS$  monolayer, alkali metal ions are more stably adsorbed on the O-terminated surfaces. The Li/Na/K ion on the surface of the Janus  $V_2COS$  monolayer demonstrates a lower diffusion barrier than other 2D materials. Lastly, we find that the Janus  $V_2COS$  monolayer exhibits a good recyclability, a larger specific capacity for Na ions, and a low OCV for K ions. It presents that the Janus  $V_2COS$  monolayer has great potential to be an anode material of SIBs and PIBs.

## ACKNOWLEDGMENTS

This work was supported by the National Natural Science Foundation of China (Grants No. 62075109, No. 62135011, and No. 61701261). The work was also supported in part by the Joint Funds of the Zhejiang Provincial Natural Science Foundation of China (Grant No. LZY22E030001) and the Natural Science Foundation of Jiangsu Province (Grant No. BK20160417). The work was also supported in part by Quzhou 115 Talent Project, and the Quzhou Science and Technology Bureau Projects (Grant No. 2023K232).

- [1] A. Qazi, F. Hussain, N. A. B. D. Rahim, G. Hardaker, D. Alhazzawi, K. Shaban, and K. Haruna, Towards sustainable energy: A systematic review of renewable energy sources, technologies, and public opinions, *IEEE Access* **7**, 63837 (2019).
- [2] G. Zubi, R. Dufo-López, M. Carvalho, and G. Pasaoglu, The lithium-ion battery: State of the art and future perspectives, *Renew. Sustain. Energy Rev.* **89**, 292 (2018).
- [3] J. B. Goodenough and K.-S. Park, The Li-ion rechargeable battery: A perspective, *J. Am. Chem. Soc.* **135**, 1167 (2013).
- [4] S. R. Taylor, Abundance of chemical elements in the continental crust: A new table, *Geochim. Cosmochim. Acta* **28**, 1273 (1964).
- [5] M. D. Slater, D. Kim, E. Lee, and C. S. Johnson, Sodium-ion battery, *Adv. Funct. Mater.* **23**, 947 (2013).
- [6] H. Kim, J. C. Kim, M. Bianchini, D.-H. Seo, J. Rodriguez-Garcia, and G. Ceder, Recent progress and perspective in electrode materials for K-ion batteries, *Adv. Energy Mater.* **8**, 1702384 (2018).
- [7] K. Sato, M. Noguchi, A. Demachi, N. Oki, and M. Endo, A mechanism of lithium storage in disordered carbons, *Science* **264**, 556 (1994).
- [8] M. Goktas, C. Bolli, E. J. Berg, P. Novák, K. Pollok, F. Langenhorst, M. v. Roeder, O. Lenchuk, D. Mollenhauer, and P. Adelhelm, Graphite as cointercalation electrode for sodium-ion battery: Electrode dynamics and the missing solid electrolyte interphase (SEI), *Adv. Energy Mater.* **8**, 1702724 (2018).
- [9] Z. Jian, W. Luo, and X. Ji, Carbon electrodes for K-ion battery, *J. Am. Chem. Soc.* **137**, 11566 (2015).
- [10] M. Mortazavi, C. Wang, J. Deng, V. B. Shenoy, and N. V. Medhekar, Ab initio characterization of layered  $MoS_2$  as anode for sodium-ion battery, *J. Power Sources* **268**, 279 (2014).
- [11] D. Su, S. Dou, and G. Wang, Ultrathin  $MoS_2$  nanosheets as anode materials for sodium-ion batteries with superior performance, *Adv. Energy Mater.* **5**, 1401205 (2015).
- [12] L. Fagiolari, D. Versaci, S. Bodoardo, and F. Bella, An exploratory study of  $MoS_2$  as anode material for potassium batteries, *Batteries* **8**, 242 (2022).
- [13] J. Jin, G. Deokar, P. M. F. J. Costa, and U. Schwingenschlög, Monolayer  $C_5N$ : A promising building block for the anode of K-ion battery, *Phys. Rev. Appl.* **17**, 034055 (2022).
- [14] Y. Li, T. Zhao, L. Li, R. Huang, and Y. Wen, Computational evaluation of ScB and TiB MBenes as promising anode materials for high-performance metal-ion battery, *Phys. Rev. Mater.* **6**, 045801 (2022).
- [15] A. Samad and U. Schwingenschlög,  $M_2X$  monolayers as anode materials for Li ion battery, *Phys. Rev. Appl.* **15**, 034025 (2021).
- [16] D. Sun, Q. Hu, J. Chen, X. Zhang, L. Wang, Q. Wu, and A. Zhou, Metallic monolayer  $Ta_2CS_2$ : An anode candidate for  $Li^+$ ,  $Na^+$ ,  $K^+$ , and  $Ca^{2+}$  ion batteries, *ACS Appl. Mater. Interfaces* **8**, 74 (2016).
- [17] Y. Wang, W. Tian, H. Zhang, and Y. Wang,  $Nb_2N$  monolayer as a promising anode material for Li/Na/K/Ca-ion battery: A DFT calculation, *Phys. Chem. Chem. Phys.* **23**, 12288 (2021).
- [18] W. Guo, Z. She, H. Xue, and X. Zhang, Density functional theory study on the  $Ti_3CN$  and  $Ti_3CNT_2$  ( $T = O, S$  and  $F$ ) as high capacity anode material for Na ion battery, *Appl. Surf. Sci.* **529**, 147180 (2020).
- [19] M. Naguib, O. Mashtalir, J. Carle, V. Presser, J. Lu, L. Hultman, Y. Gogotsi, and M. W. Barsoum, Two-dimensional transition metal carbides, *ACS Nano* **6**, 1322 (2012).
- [20] X. Yang, X. Zhang, Z. Lu, Z. Yang, and R. Wu, Design of highly stable and efficient bifunctional MXene-based electrocatalysts for oxygen reduction and evolution reactions, *Phys. Rev. Appl.* **15**, 044053 (2021).
- [21] S. Nyamdelger, T. Ochirkhuyag, D. Sangaac, and D. Odkhuu, First-principles prediction of a two-dimensional vanadium carbide (MXene) as the anode for lithium ion battery, *Phys. Chem. Chem. Phys.* **22**, 5807 (2020).
- [22] Y.-M. Li, Y.-L. Guo, and Z.-Y. Jiao, The effect of S-functionalized and vacancies on  $V_2C$  MXenes as anode materials for Na-ion and Li-ion battery, *Curr. Appl. Phys.* **20**, 310 (2020).
- [23] S. Wang, Y. Wang, Q. Zhou, X. Li, Y. Li, Y. Liu, Y. Sun, T. Wang, L.-C. Xu, and Y. Wang, Modelling high performance potassium-ion battery anode materials with two-dimensional vanadium carbide MXene: The role of surface O- and S-terminations, *Phys. Chem. Chem. Phys.* **23**, 3898 (2021).
- [24] J. Zhang, S. Jia, I. Kholmanov, L. Dong, D. Er, W. Chen, H. Guo, Z. Jin, V. B. Shenoy, L. Shi, and J. Lou, Janus monolayer transition-metal dichalcogenides, *ACS Nano* **11**, 8192 (2017).
- [25] G. Chaney, A. Ibrahim, F. Ersan, D. Çakır, and C. Ataca, Comprehensive study of lithium adsorption and diffusion on Janus Mo/WXY ( $X, Y = S, Se, Te$ ) using first-principles and machine learning approaches, *ACS Appl. Mater. Interfaces* **13**, 36388 (2021).
- [26] F. Xiong and Y. Chen, A first-principles study of Janus monolayer TiSSe and VSSe as anode materials in alkali metal ion battery, *Nanotechnology* **32**, 25702 (2021).
- [27] S. Lei, X. Chen, J. Wen, X. Zhou, and B. Xiao, Passivated 2D Janus borophene as unique Dirac anodes for Na- and K-ion battery: A first-principle investigation, *Appl. Surf. Sci.* **578**, 151994 (2022).

- [28] X. Tang, H. Ye, W. Liu, Y. Liu, Z. Guo, and M. Wang, Lattice-distorted lithiation behavior of a square phase Janus MoSSe monolayer for electrode applications, *Nanoscale Adv.* **3**, 2902 (2021).
- [29] E. M. D. Siriwardane and J. Hu, First-principles investigation of Ti<sub>2</sub>CSO and Ti<sub>2</sub>CSSe Janus MXene structures for Li and Mg electrodes, *J. Phys. Chem. C* **125**, 12469 (2021).
- [30] S. Özcan and B. Biel, Sc<sub>2</sub>CX (X = N<sub>2</sub>, ON, O<sub>2</sub>) MXenes as a promising anode material: A first-principles study, *J. Appl. Phys.* **133**, 44301 (2023).
- [31] Z. Bao, C. Lu, X. Cao, P. Zhang, L. Yang, H. Zhang, D. Sha, W. He, W. Zhang, and L. Pan, Role of MXene surface terminations in electrochemical energy storage: A review, *Chin. Chem. Lett.* **32**, 2648 (2021).
- [32] S. Zhao, X. Luo, Y. Cheng, Z. Shi, T. Huang, S. Yang, H. Zheng, Y. Bi, J. Zhang, Q. Shi, M. Cao, C. Zhang, Y. Yue, and Y. Ma, A flexible zinc ion hybrid capacitor integrated system with layers-dependent V<sub>2</sub>CTx MXene, *Chem. Eng. J.* **454**, 140360 (2023).
- [33] Y. Zhang, Y. Jiang, Z. Duan, Q. Huang, Y. Wu, B. Liu, Q. Zhao, S. Wang, Z. Yuan, and H. Tai, Highly sensitive and selective NO<sub>2</sub> sensor of alkalized V<sub>2</sub>CT MXene driven by interlayer swelling, *Sens. Actuators B* **344**, 130150 (2021).
- [34] Y. Liu, Y. Jiang, Z. Hu, J. Peng, W. Lai, D. Wu, S. Zuo, J. Zhang, B. Chen, Z. Dai, Y. Yang, Y. Huang, W. Zhang, W. Zhao, W. Zhang, L. Wang, and S. Chou, In-situ electrochemically activated surface vanadium valence in V<sub>2</sub>C MXene to achieve high capacity and superior rate performance for Zn-ion batteries, *Adv. Funct. Mater.* **31**, 2008033 (2021).
- [35] L. Zhang, Y. Xia, X. Li, L. Li, X. Fu, J. Cheng, and R. Pan, Janus two-dimensional transition metal dichalcogenides, *J. Appl. Phys.* **131**, 230902 (2022).
- [36] S. Smidstrup, T. Markussen, P. Vancraeyveld, J. Wellendorff, J. Schneider, T. Gunst, B. Verstichel, D. Stradi, P. A. Khomyakov, U. G. Vej-Hansen *et al.*, QuantumATK: An integrated platform of electronic and atomic-scale modelling tools, *J. Phys.: Condens. Matter* **32**, 15901 (2020).
- [37] J. P. Perdew, K. Burke, and M. Ernzerhof, Generalized gradient approximation made simple, *Phys. Rev. Lett.* **77**, 3865 (1996).
- [38] S. Grimme, J. Antony, S. Ehrlich, and H. Krieg, A consistent and accurate ab initio parametrization of density functional dispersion correction (DFT-D) for the 94 elements H-Pu, *J. Chem. Phys.* **132**, 154104 (2010).
- [39] J. Moellmann and S. Grimme, DFT-D3 study of some molecular crystals, *J. Phys. Chem. C* **118**, 7615 (2014).
- [40] P. Negro, F. Cesano, S. Casassa, and D. Scarano, Combined DFT-D3 computational and experimental studies on g-C<sub>3</sub>N<sub>4</sub>: New insight into structure, optical, and vibrational properties, *Materials* **16**, 3644 (2023).
- [41] D. J. Chadi, Special points for Brillouin-zone integrations, *Phys. Rev. B* **16**, 1746 (1977).
- [42] See Supplemental Material at <http://link.aps.org/supplemental/10.1103/PhysRevMaterials.8.085801> for the AIMD simulations, calculation method of elastic constant, multilayer adsorption configurations, and the side view of V<sub>2</sub>COS supercell with maximum adsorbed alkali metal ions.
- [43] G. J. Martyna, M. L. Klein, and M. Tuckerman, Nosé-Hoover chains: The canonical ensemble via continuous dynamics, *J. Chem. Phys.* **97**, 2635 (1992).
- [44] G. Henkelman, B. P. Uberuaga, and H. Jónsson, A climbing image nudged elastic band method for finding saddle points and minimum energy paths, *J. Chem. Phys.* **113**, 9901 (2000).
- [45] J. Yue, J. Zheng, J. Li, S. Guo, W. Ren, H. Liu, Y. Liu, and T. Cui, Ultralow glassy thermal conductivity and controllable, promising thermoelectric properties in crystalline o-CsCu<sub>5</sub>S<sub>3</sub>, *ACS Appl. Mater. Interfaces* **16**, 20597 (2024).
- [46] J. Yue, Y. Liu, W. Ren, S. Lin, C. Shen, H. K. Singh, T. Cui, T. Tadano, and H. Zhang, Role of atypical temperature-responsive lattice thermal transport on the thermoelectric properties of antiperovskites Mg<sub>3</sub>XN (X = P, As, Sb, Bi), *Mater. Today Phys.* **41**, 101340 (2024).
- [47] Y. Le Page and P. Saxe, Symmetry-general least-squares extraction of elastic data for strained materials from *ab initio* calculations of stress, *Phys. Rev. B* **65**, 104104 (2002).
- [48] C. Jasiukiewicz, T. Paszkiewicz, and S. Wolski, Auxetic properties and anisotropy of elastic material constants of 2D crystalline media, *Phys. Status Solidi B* **245**, 562 (2008).
- [49] Z. Li and F. Cheng, C<sub>3</sub>Al: A tunable bandgap semiconductor with high electron mobility and negative Poisson's ratio, *Phys. E* **138**, 115082 (2022).
- [50] Z. Li and F. Cheng, First-principles study on the mechanical and electromagnetic properties of porous two-dimensional C<sub>7</sub>N<sub>2</sub> crystals, *Phys. E (Amsterdam, Neth.)* **132**, 114758 (2021).
- [51] Y. Wang, J. Shen, L. Xu, Z. Yang, R. Li, R. Liu, and X. Lia, Sulfur-functionalized vanadium carbide MXene (V<sub>2</sub>CS<sub>2</sub>) as a promising anchoring material for lithium-sulfur battery, *Phys. Chem. Chem. Phys.* **21**, 18559 (2019).
- [52] M. Kim, W. J. Kim, T. Gould, E. K. Lee, S. Lebègue, and H. Kim, uMBD: A materials-ready dispersion correction that uniformly treats metallic, ionic, and van der Waals bonding, *J. Am. Chem. Soc.* **142**, 2346 (2020).
- [53] R. S. Mulliken, Electronic population analysis on LCAO-MO molecular wave functions. I, *J. Chem. Phys.* **23**, 1833 (1955).
- [54] Y. Chen, J. Liu, M. Ju, R. Qiu, and H. Yuan, Magnetic stability of Ce and Nd single atom magnets on insulating MgO/Ag (100), *Phys. Rev. B* **107**, 214444 (2023).
- [55] M. I. Khan, G. Nadeem, A. Majid, and M. Shakil, A DFT study of bismuthene as anode material for alkali-metal (Li/Na/K)-ion battery, *Mater. Sci. Eng. B* **266**, 115061 (2021).
- [56] K. Toyoura, Y. Koyama, A. Kuwabara, F. Oba, and I. Tanaka, First-principles approach to chemical diffusion of lithium atoms in a graphite intercalation compound, *Phys. Rev. B* **78**, 214303 (2008).
- [57] B. Yan, C. Lu, P. Zhang, J. Chen, W. He, W. Tian, W. Zhang, and Z. Sun, Oxygen/sulfur decorated 2D MXene V<sub>2</sub>C for promising lithium ion battery anodes, *Mater. Today Commun.* **22**, 100713 (2020).
- [58] M. Debbichi, A. Mallah, M. H. Dhaou, and S. Lebègue, First-principles study of monolayer *pent-a*-CoS<sub>2</sub> as a promising anode material for Li/Na-ion battery, *Phys. Rev. Appl.* **16**, 024016 (2021).
- [59] A. Kokalj, Formation and structure of inhibitive molecular film of imidazole on iron surface, *Corros. Sci.* **68**, 195 (2013).
- [60] N. Li, Y. Li, X. Zhu, C. Huang, J.-J. Kai, and J. Fan, Theoretical investigation of the structure-property correlation of MXenes as anode materials for alkali metal ion battery, *J. Phys. Chem. C* **124**, 14978 (2020).

- [61] T. Bai, H. Liu, B. Chen, Y. Qiu, H. Dong, K. Wu, Y. Cheng, and B. Xiao, Assessing  $(\text{Mo}_{2/3}\text{Sc}_{1/3})_2\text{C}$  and  $(\text{Mo}_{2/3}\text{Sc}_{1/3})_2\text{CT}_2$  ( $T = -\text{O}, -\text{OH}, \text{and } -\text{F}$ ) i-MXenes as high-performance electrode materials for lithium and non-lithium ion Battery, *J. Phys. Chem. C* **126**, 10273 (2022).
- [62] Z. Liu, H. Deng, and P. P. Mukherjee, Evaluating pristine and modified  $\text{SnS}_2$  as a lithium-ion battery anode: A first-principles study, *ACS Appl. Mater. Interfaces* **7**, 4000 (2015).
- [63] A. N. Enyashin and G. Seifert, Density-functional study of  $\text{Li}_x\text{MoS}_2$  intercalates ( $0 \leq x \leq 1$ ), *Comput. Theor. Chem.* **999**, 13 (2012).
- [64] X. Zhang, Z. Zhang, S. Yao, An Chen, X. Zhao, and Z. Zhou, An effective method to screen sodium-based layered materials for sodium ion batteries, *npj Comput. Mater.* **4**, 13 (2018).
- [65] D. Er, J. Li, M. Naguib, Y. Gogotsi, and V. B. Shenoy,  $\text{Ti}_3\text{C}_2$  MXene as a high capacity electrode material for metal (Li, Na, K, Ca) ion battery, *ACS Appl. Mater. Interfaces* **6**, 11173 (2014).
- [66] Y. Wang, Y. Ma, Q. Zhang, R. Huang, B. Gao, Z. Li, G. Li, and F. Liang, First-principles investigation of  $\text{V}_2\text{CSe}_2$  MXene as a potential anode material for non-lithium metal ion batteries, *Curr. Appl. Phys.* **41**, 7 (2022).
- [67] Y. Li, L. Bai, N. Ma, and L. Niu, O- or/and S-functionalized  $\text{Cr}_2\text{C}$  as electrode material for metal-ion (Li, Na, K, and Mg) batteries: A first principles study, *Comput. Theor. Chem.* **1217**, 113892 (2022).
- [68] S. Ahmad, H. U. Din, S. Nawaz, S. Nguyen, C. Q. Nguyen, and C. V. Nguyen, First principles study of the adsorption of alkali metal ions (Li, Na, and K) on Janus WSSe monolayer for rechargeable metal-ion battery, *Appl. Surf. Sci.* **632**, 157545 (2023).
- [69] H. Wang, Q. Chen, H. Lia, Q. Duan, D. Jiang, and J. Hou, Two-dimensional Janus MoSSe as a potential anode material for Na/K-ion batteries: A theoretical study, *Chem. Phys. Lett.* **735**, 136777 (2019).
- [70] C. Shang, X. Lei, B. Hou, M. Wu, B. Xu, G. Liu, and C. Ouyang, Theoretical prediction of Janus MoSSe as a potential anode material for lithium-ion battery, *J. Phys. Chem. C* **122**, 23899 (2018).
- [71] Y. Cui, H. Qin, P. Kong, J. Chen, X. Cai, and Y. Chen, Exploring a novel two-dimensional metallic  $\text{Y}_4\text{C}_3$  sheet applied as an anode material for sodium-ion battery, *Phys. Chem. Chem. Phys.* **24**, 8859 (2022).
- [72] X.-Y. Yang, W. Luo, and R. Ahuja, Fluoride ion batteries: Designing flexible  $\text{M}_2\text{CH}_2$  ( $M = \text{Ti}$  or  $\text{V}$ ) MXenes as high-capacity cathode materials, *Nano Energy* **74**, 104911 (2020).
- [73] Y. Jing, Jie Liu, Z. Zhou, J. Zhang, and Y. Li, Metallic  $\text{Nb}_2\text{S}_2\text{C}$  monolayer: A promising two-dimensional anode material for metal-ion battery, *J. Phys. Chem. C* **123**, 26803 (2019).
- [74] Q.-Y. Wu, T.-L. Zhao, X.-J. Ye, H. Lin, X.-H. Zheng, R. Jia, and C.-S. Liu, Theoretical prediction of metallic R12-graphene as a promising anode material for potassium-ion battery with high ion mobility, high capacity, and excellent electrolyte wettability, *Appl. Phys. Lett.* **123**, 093902 (2023).
- [75] Y. Zhou, Y. Han, H. Zhang, D. Sui, Z. Sun, P. Xiao, X. Wang, Y. Ma, and Y. Chen, A carbon cloth-based lithium composite anode for high-performance lithium metal batteries, *Energy Storage Mater.* **14**, 222 (2018).
- [76] P. Zhu, D. Gastol, J. Marshall, R. Sommerville, V. Goodship, and E. Kendrick, A review of current collectors for lithium-ion batteries, *J. Power Sources* **485**, 229321 (2021).